Research Square

Preprints are preliminary reports that have not undergone peer review.
They should not be considered conclusive, used to inform clinical practice,
or referenced by the media as validated information.

Gut microbiota ablation depletes secondary bile acids and shifts the cytokine balance in BCG-infected mice

Yujie Ma
Shihezi University
Lili Zhu
Xinjiang Second Medical College
Yu Xie
Shihezi University
Yuxuan Gou
Xinjiang Second Medical College
Beiming Zhang
Xinjiang Hospital of Beijing Children's Hospital, Children's Hospital of Xinjiang Uygur Autonomous Region, The Seventh People's Hospital of Xinjiang Uygur Autonomous Region CN
Rong Zhang
Xinjiang Second Medical College
Chunhong Xiao
Xinjiang Second Medical College
Jing Chen
Xinjiang Second Medical College
Le Zhang
Shihezi University
Jiangdong Wu
1556874645@qq.com

Xinjiang Second Medical College
Qifeng Li
Xinjiang Hospital of Beijing Children's Hospital, Children's Hospital of Xinjiang Uygur Autonomous Region, The Seventh People's Hospital of Xinjiang Uygur Autonomous Region CN

Research Article

Keywords: gut microbiota, antibiotic ablation, secondary bile acids, BCG, metagenomics, metabolomics, cytokines

Posted Date: November 2nd, 2026

DOI: https://doi.org/10.21203/rs.3.rs-11140836/v1

License: This work is licensed under a Creative Commons Attribution 4.0 International License.
Read Full License

Additional Declarations: No competing interests reported.

Abstract

Background. Antibiotic ablation is the standard test of whether a host phenotype depends on the gut microbiota, but it removes the community and perturbs the host at once, so depletion alone cannot assign a metabolite shift to the community. We built a four-arm mouse model on a single BCG infection background: untreated controls (NC), BCG alone, BCG after mixed-antibiotic ablation (ABX_BCG), and BCG followed by faecal microbiota transplantation with no antibiotic exposure at any point (BCG_FMT). The ablated and transplanted arms were independent branches, not a depletion-then-restoration sequence.

Results. Dual-polarity untargeted LC-MS (9,706 negative-mode and 11,589 positive-mode features) and shotgun metagenomics showed that ablation left a block of 726 negative-mode and 313 positive-mode features absent from all three ABX_BCG samples but detected in 88–94% of the other nine; total ion signal in the ablated arm exceeded that of the quality-control injections, excluding dilution and matrix loss. Twenty-seven block features were annotated, resolving to 17 unique InChIKeys, 21 of them microbial compound classes including secondary bile acids. Deoxycholic acid eluted at 437.93 s in negative mode and 437.28 s in positive mode; deoxycholic and lithocholic acid were undetected in the ablated samples. Both omics layers resolved the same four groups (PERMANOVA $R^2 = 0.562$ for the genus table and 0.635 for the metabolome) yet failed to couple at sample level; exhaustive within-group re-pairing excluded sample mismatch, identifying a shared treatment rather than an individual axis. Ablation accompanied higher TNF-α and IL-6 and lower IFN-γ and IL-10 in bronchoalveolar lavage fluid and serum alike.

Conclusions. The gut community contributes a set of metabolite features whose absence is specific to the ablated state rather than shared with infection or transplantation, and the same arm occupies the extreme of the cytokine readout in both compartments. Running the ablated and transplanted arms as independent branches off the infected baseline is what makes this an antibiotic-specific control, and the two omics layers carry a shared treatment structure rather than a shared individual axis.

Introduction

The intestinal microbiota calibrates immune tone at distal mucosal surfaces, and the lung is one of the compartments that register that calibration.[1,2] Animals raised without a gut community, or depleted of one by antibiotics, differ from conventional animals in the composition and activation state of pulmonary myeloid and lymphoid populations,[3,4] and the effect is large enough that community composition is now treated as a variable in models of respiratory infection and of vaccine responses.[5,6] BCG is one such model. The live attenuated bacillus is both the standard experimental challenge in murine tuberculosis research and the oldest vaccine still in use,[7,8] and the immune response it elicits is read out in the lung and in the circulation — two compartments that are exposed to whatever microbial products the intestine releases into the systemic pool.[9]

Antibiotic ablation is the workhorse for asking whether a phenotype depends on the microbiota, and its weakness is well known but rarely confronted head-on.[10] An antibiotic cocktail does not remove the community in isolation. It also shifts host physiology, rewrites the chemistry of the intestinal lumen,[11,12] and in some cases acts on host cells directly.[13] A metabolite that disappears after ablation may therefore have been lost because the bacteria that made it are gone, or because the antibiotic changed the tissue that absorbed, conjugated or excreted it. Depletion on its own buys an association with the treatment, not an assignment to the community.

The usual remedy is to add the community back. Faecal microbiota transplantation after ablation, or colonisation of germ-free animals with a defined consortium, is read as evidence that the community is responsible for the phenotype in question.[14,15] Both designs carry a cost of their own. Restoration designs compare every arm against a shared reference, which builds a structural correlation between the contrasts that owes nothing to biology, and they collapse two manipulations — removal and reintroduction — onto a single axis, so the specificity of the depleted state is never tested against a transplanted state that was never depleted.[16]

We built that comparison into the design. Four arms of mice shared one BCG infection background: untreated controls (NC), infection alone (BCG), infection after mixed-antibiotic ablation of the gut community (ABX_BCG), and infection followed by faecal microbiota transplantation with no antibiotic exposure at any point (BCG_FMT). The ablated and transplanted arms were independent branches off the infected baseline rather than successive stages of one procedure.[17] We profiled all four arms with shotgun metagenomics and dual-polarity untargeted LC-MS, and read four cytokines in bronchoalveolar lavage fluid and in serum. Two questions organise the analysis. The first is whether ablation leaves a metabolite signature that is specific to the ablated arm rather than shared with infection or with transplantation; the answer turned out to be a block of features defined by detection rather than by effect size, which is the central result reported here. The second is how far the metagenomic and metabolomic layers agree, and at which level of organisation that agreement holds.

Results

R1. The four arms differ in community structure and in functional potential

Twelve mice were assigned to four arms of three animals each, all carrying the same BCG infection background. Relative abundance profiles at phylum, class and genus level separated the arms instead of resolving them onto a single gradient, and the separation was visible both in group-level summaries and in the twelve individual libraries. Diversity was profiled in the three arms that retained a detectable community; the ablated arm, by construction, has no community to profile. Shannon indices in those three arms spanned 4.5 to 6.0 and observed species counts spanned 8,000 to 10,000. Ordination of genus-level Bray–Curtis dissimilarities placed the three community-bearing arms in distinct regions of the plane, with PCoA1 accounting for 46.8% and PCoA2 for 30.4% of the variance, and permutational multivariate analysis of variance confirmed the separation ($R^2 = 0.51$, $P = 0.0057$) (Figure 1).

The functional layer followed the same partition. Of the fourteen KEGG level-3 pathways retained for display, several sit directly on fermentation and bile-acid chemistry: butanoate metabolism, propanoate metabolism, pyruvate metabolism, other carbon fixation pathways, methane metabolism, glycolysis/gluconeogenesis, the citrate cycle, starch and sucrose metabolism, amino sugar and nucleotide sugar metabolism, fructose and mannose metabolism, the pentose phosphate pathway, primary bile acid biosynthesis, secondary bile acid biosynthesis, and tryptophan metabolism. Row-scaled abundances of these pathways varied systematically across the twelve samples, with the ablated arm summarised by a mean column, and the ordering of the arms they produced matched the taxonomic ordering. Differential scoring across the six taxonomic ranks from phylum to species identified taxa whose between-arm separation exceeded the within-arm spread, and genus-level effect sizes against the untreated control were carried by a small number of genera rather than distributed evenly across the community (Figure 1). At this level of description the four arms differ in community structure and in the functional potential that accompanies it. These profiles are not, on their own, an argument about causality.

R2. Contrast-specific effect sets differ in size and in composition

We defined three contrasts against the infected baseline and its untreated control: S1 (BCG versus NC), S2 (ABX_BCG versus BCG) and S3 (BCG_FMT versus BCG). Counting features that passed the differential threshold of FDR < 0.05 and |log2FC| ≥ 1 gave effect sets of very different sizes depending on which arm was compared. In negative mode, S1 comprised 60 features (18 up, 42 down), S2 comprised 391 (158 up, 233 down), and S3 comprised 46 (34 up, 12 down). In positive mode the corresponding sets were 41 (7 up, 34 down), 352 (142 up, 210 down) and 45 (37 up, 8 down). The antibiotic contrast therefore carried roughly an order of magnitude more responding features than either the infection contrast or the transplant contrast. Summing the seven intersection combinations of the display recovered 2,932 features in negative mode and 3,709 in positive mode, equal to the totals entered into that display; the largest set dominated it, and stem length was drawn on a square-root scale for that reason (Figure 2).

Lactate was detected in negative-ion mode at m/z 89.0251 with a retention time of 67.0 s and a mass error of +7.9 ppm. Its identification rests on accurate mass and retention time alone: no MS/MS library match was obtained, and the compound is therefore reported as an accurate-mass-and-retention-time annotation rather than a confirmed identification. Its confidence level under the Metabolomics Standards Initiative scheme is Level 2 (putatively annotated): annotation rests on accurate mass and retention time, with no comparison against an authentic chemical standard and no MS/MS library match.

The composition of these sets mattered as much as their size. S1 was dominated by losses of bile acids and lysophospholipids: taurocholic acid (two features) and cholic acid fell, and LPC 18:2 (two features), LPE 18:2 (two features) and LPC 18:1 dropped by three to six log2 units, alongside gains in 16-hydroxypalmitic acid (two features). The positive-mode side of S1 added further cholic acid losses (two features) and LPC 18:2 losses (three features).

S2 split sharply by polarity. In negative mode, taurocholic acid rose by +6.2 and +5.8 log2 units, and sinapic acid, genistein (two features) and enterolactone also rose, while 4-hydroxybenzaldehyde (two features), sebacic acid, pantothenic acid and 12-hydroxystearic acid (two features) fell. The positive-mode side of S2 was more categorical: microbial nucleosides and aromatic compounds were cleared, with losses in tyrosine (two features), adenosine, uridine, nicotinic acid, uracil (two features), xanthine, thymine, pipecolic acid (two features) and deoxyadenosine, while sucrose and raffinose rose and taurocholic acid gained across three features. S3 was both smaller and differently composed, with gains in lysophospholipids, soyasaponin and cholic acid, and losses of inosine and uridine (Figure 3).

R3. The analysed feature set is analytically sound and explicitly bounded

Feature extraction returned 9,706 features in negative mode and 11,589 in positive mode, capturing 90.8% and 96.6% of quality-control signal respectively. Two processing decisions govern how everything downstream should be read. The first concerns sample ordering. Ranking samples on a matrix in which undetected values have been replaced by a detection-limit surrogate displaces the quality-control injections — which detect every feature — to the positive end of each missingness axis, and they then appear to sit 64.2 (negative mode) and 70.3 (positive mode) units from the nearest group centroid while the instrument was in fact stable. We therefore ordered samples on complete-case features only, restricted to those detected across all fifteen injections: 431 features in negative mode and 783 in positive mode. On that basis within-quality-control dispersion was 0.13 against within-group dispersions of 1.15–4.36 in negative mode, and 0.31 against 3.17–6.46 in positive mode. The second decision concerns normalisation. Probabilistic quotient normalisation factors were measured rather than assumed to be neutral across groups, and they spanned 0.800–1.009 (NC), 0.906–1.182 (BCG), 1.000–1.032 (ABX_BCG), 1.051–1.190 (BCG_FMT) and 0.985–1.000 (QC) in negative mode, and 0.867–1.001 (NC), 0.895–1.080 (BCG), 0.954–1.000 (ABX_BCG), 1.018–1.115 (BCG_FMT) and 1.000–1.032 (QC) in positive mode. No group served as a normalisation reference (Figure 2).

The boundary of the analysis window belongs in the same place, at the point where results are first used. The lowest recorded m/z was 71.0 in negative mode and 57.0 in positive mode, and that floor has consequences for two compound classes of interest. Short-chain fatty acids and polyamines do not appear in the feature table at all, and the reasons differ by class and by channel. In negative mode, the lowest recorded m/z of 71.0 sits 22,700 ppm away from the nearest short-chain fatty acid ion, far outside the 10 ppm window applied there, so the exclusion is a matter of mass and nothing else. In positive mode the lowest recorded m/z of 57.0 is within 24.7 ppm of the nearest candidate, which is close enough on mass alone to be admissible inside the 20 ppm window; that candidate, however, elutes at 6.5 min, whereas the small polar acids that were actually measured — lactate at 0.6, 0.9 and 1.1 min, malate at 0.65 min and 2-oxoglutarate at 1.05 min — have all eluted before 1.1 min. The exclusion there is therefore made on retention time, not on mass. The two classes are absent because of where the analytical window sits, and we state the mechanism of exclusion rather than treating the absence as a biological result (Figure 2).

R4. Ablation leaves a metabolite block that no ablated sample contains

Inside the S2 effect set sits a group of features distinguished not by effect size but by detection. In negative mode 726 features, and in positive mode 313 features, were recorded at 0.0% in all three ABX_BCG samples while being detected at rates of 88–91% in NC, 91–94% in BCG and 93–94% in BCG_FMT. The block therefore has a detection profile of roughly 0.9, 0.9, 0.0 and 0.9 across the four arms, and it accounts for 10.0% of total signal in negative mode and 0.9% in positive mode. Its absence is not a sampling or suppression artefact. Total ion signal in the ABX_BCG samples was higher than in the quality-control injections ($1.82–2.38 \times 10^8$ versus $1.61–1.72 \times 10^8$), which excludes the two obvious explanations for a wholesale loss of signal in one arm: dilution of the injected material, and matrix suppression at the source (Figures 2, 3).

The specificity of the block is what the design was built to test. It is present in the untreated control, in infection alone, and in infection followed by transplantation; it is absent only where the community was ablated. That pattern makes it an antibiotic-specific control for the role of the microbiota rather than a correlate of infection or of transplantation, and it is the reason the ablated and transplanted arms were placed on separate branches rather than run as successive stages of one procedure. One alternative reading is excluded by the detection pattern itself. If the block were a general consequence of the infected state, it would also be depleted in the transplanted arm or in the infected baseline; it is depleted in neither.

R5. Annotation assigns the block to microbial compound classes

Annotation narrowed the block to 27 features, 13 from negative mode and 14 from positive mode, resolving to 17 unique InChIKeys. Twenty-one of the 27 belong to compound classes of microbial origin. The negative-mode annotations comprised seven bile acids — deoxycholic acid (three features), 3-dehydrocholic acid (three features) and chenodeoxycholic acid — together with three dicarboxylic acids, two lipids and one organic acid (malate). The positive-mode annotations comprised five bile acids, three cofactors and two microbial lignans, and included deoxycholic acid, cholic acid, enterolactone (two features), ferulic acid, adenine (two features), pyridoxine and oleoylethanolamine (Figure 2).

One annotation is supported independently by both acquisition channels. Deoxycholic acid eluted at 437.93 s in negative mode and at 437.28 s in positive mode, a difference of well under a second across two separately acquired methods. Two features that entered annotation were discarded as artefacts rather than reported: a deuterated internal standard, DHA-[d5], and the corrosion inhibitor 5-methylbenzotriazole. The block is thus not a mixture of unrelated compounds but a set of molecules whose shared property is that they are products or substrates of intestinal microbial transformation.

R6. Associations between taxa and metabolites are dominated by a compact set of strong pairs

Genus-level abundance and metabolite intensity were correlated across all twelve samples. The result was not a broad field of weak associations but a compact set of strong ones, and that set behaved

consistently under the removal of the ablated arm. The strongest associations were the strongest either way: Candidatus_Homeothermus against negative-mode feature F2747 moved from +0.904 to +0.817 when the three ABX_BCG samples were dropped; Barnesiella against positive-mode F11728 from +0.886 to +0.900; Lactobacillus against positive-mode F9331 from +0.883 to +0.917; and Lepagella against negative-mode F7954 from −0.873 to −0.967. Association strengths of this magnitude sit well past the significance threshold at this sample size, which is $|\rho| \geq 0.577$ for twelve samples and $|\rho| \geq 0.667$ for nine (Figures 4, 5).

We tested how much of the correlation field depended on the ablated arm. Restricting the scan to the nine samples that retained a detectable metabolome left 473 pairs significant, 35.2% of those found in the full scan, and every one of the 473 kept its sign. That restricted set is what we report; the remainder of the correlation field is treated as unresolved, because at this sample size a long tail of weaker associations cannot be separated from the structural consequences of a three-sample arm whose metabolome is degenerate by construction (Figure 5).

R7. The targeted layer isolates secondary bile acids, and states its own coverage

The targeted layer provides the sharpest single piece of evidence for the block. Secondary bile acids — deoxycholic acid and lithocholic acid among them — were undetected in all three ABX_BCG samples and detected in every sample of the other three arms. Deoxycholic acid and chenodeoxycholic acid share an identical m/z of 391.2828 and an identical retention time of 437.9 s and are therefore isomers of one another; they are reported once, as an isomer pair, and flagged as such in the display. Targeted scoring was unambiguous in negative mode, where tryptophan (0.974), taurocholate (0.972), cholate (0.953), the deoxycholate/chenodeoxycholate pair (0.945) and malate (0.747) all exceeded a score of 0.70. No positive-mode target reached that level: indole-3-aldehyde (0.675), cholate (0.539) and indole (0.369) all fell below it (Figure 4).

One analyte deserves separate mention because it sits at the edge of the analytical window. Lactate was detected in negative mode at m/z 89.0251 with a retention time of 67.0 s and a mass error of +7.9 ppm, and its intensity differed across the four arms (Kruskal–Wallis $P = 0.047$). Identification rests on accurate mass and retention time; the qualitative tier at which it is reported is set out in the Methods and in the figure legend (Figure 2).

R8. The two omics layers agree at group level and decouple at sample level

The two layers were assessed for agreement at two levels that are often conflated. At group level they agreed closely. Permutational multivariate analysis of variance on the genus table gave $R^2 = 0.562$ ($P = 0.0009$), and the same test on the all-feature metabolome under total-sum scaling and Bray–Curtis gave $R^2 = 0.635$ ($P = 0.0003$–0.0006). Both layers therefore recover the same four-group structure with comparable strength. At sample level the picture differs, and it is printed on the display: the primary ordination panel reports a Mantel statistic of $r = −0.10$ ($P = 0.657$) and a Procrustes statistic of $r = 0.27$ ($P = 0.690$) (Figure 5).

Alternative constructions do not change the sample-level result. Procrustes agreement was 0.299 (P = 0.59) when restricted to features detected in at least six of twelve samples, 0.377 (P = 0.30) on a flora-dependent Euclidean log10 scale, 0.391 (P = 0.42) when only the nine non-ablated samples were used, and 0.461 (P = 0.29) when both restrictions were applied together. Nor is the low agreement an artefact of mispaired samples. We enumerated all 6^4 = 1,296 possible within-group reassignments of the twelve animals and computed the Procrustes statistic for each: the median was 0.290, the maximum was 0.351, and no reassignment reached 0.8. No pairing of the available samples, correct or incorrect, produces sample-level coupling. The appropriate reading is that the two layers carry a shared treatment structure rather than a shared individual axis, which is a property of this system under this design rather than a failure of integration. One definitional point belongs here: the flora-dependent subset, by construction the features that collapse under ablation, is zero across all three ABX_BCG samples, so its Bray–Curtis sample rows are degenerate and the ordination panel must be, and is, built on the full-feature matrix.

R9. The cytokine readout moves with ablation in both compartments

The final block of Figure 5 reports eight ELISAs covering four analytes in two compartments, bronchoalveolar lavage fluid and serum, with three animals per arm in each. The analytes were the pro-inflammatory cytokines IFN-γ, TNF-α and IL-6, and the regulatory cytokine IL-10. Direction was consistent across the panel. ABX_BCG was the lowest arm for IFN-γ and for IL-10, and the highest arm for TNF-α and for IL-6; the transplanted arm sat on the opposite side of the infected baseline for the same four analytes. Lung and blood agreed in direction, so the shift registered both in the compartment where the infection resides and in the circulation. Every planned contrast reached significance. The single exception to the highest level was the BCG versus ABX_BCG comparison for serum TNF-α, which was significant at the $P < 0.01$ level while the remaining contrasts reached $P < 0.001$; no contrast was non-significant. Absolute concentrations for every animal and analyte are provided in the source data file submitted with the manuscript.

Discussion

The central advance of this work is a metabolite signature defined by detection rather than by effect size. Mixed-antibiotic ablation of the gut community left 726 negative-mode and 313 positive-mode features that were recorded at 0.0% in all three ablated samples and detected in 88–94% of the other nine, a pattern that no effect-size ranking would have surfaced, because a feature that is absent rather than reduced has no log2 fold change to rank. Two features of the design make this block interpretable. Because the ablated and transplanted arms were independent branches off the same infected baseline rather than successive stages of one procedure, the transplanted arm functions as a specificity control: an antibiotic-specific loss cannot be attributed to infection, and it cannot be attributed to transplantation either, since the transplanted arm never received an antibiotic.[18,19]

The annotated content of the block points in one direction. Twenty-one of the 27 annotated features belong to compound classes of microbial origin, and the recurring themes are bile-acid transformation, dicarboxylic acids, and lignan metabolism. Secondary bile acids are not synthesised by the host; they are produced when intestinal bacteria dehydroxylate primary bile acids, and deoxycholic and lithocholic acid are the canonical products of that reaction.[20–24] Enterolactone is a mammalian lignan generated by gut bacteria from plant lignan precursors, and its appearance in the annotation alongside ferulic acid places the block squarely within microbial aromatic metabolism.[25–27] That these molecules vanish together, in all three ablated samples and in none of the other nine, is what one would expect if a community-wide biotransformation capacity had been removed rather than if individual pathways had been shifted.

The rival explanations for a wholesale loss of signal in one arm were addressed in the data rather than argued away. Dilution of the injected material and matrix suppression at the source both predict lower total ion signal in the affected arm; the ablated samples carried more total ion signal than the quality-control injections, so neither prediction holds. A second rival explanation, that the block is an artefact of peak extraction or of annotation, is weakened by the cross-channel agreement on deoxycholic acid, which was detected at 437.93 s in negative mode and 437.28 s in positive mode, and by the removal of the two features that annotation flagged as artefacts. The targeted layer makes the same point with a chemically defined readout: secondary bile acids were undetected in all three ablated samples and detected in every sample of the other three arms.[28–31]

The relation to prior work lies in what the design does and does not license. Depletion designs establish that a phenotype tracks the treatment; restoration designs add the community back and read the return of the phenotype as evidence for the community. The present design does something narrower and, for this question, firmer: it holds infection constant across four arms and varies only whether the community was ablated, which lets the ablated state be contrasted against a transplanted state that never experienced the antibiotic. Within that frame we found no evidence that transplantation reverses the metabolite displacement produced by ablation. The claim we advance is therefore about the specificity of the ablated state, not about the restorability of the conventional state.

The integration result needs careful statement, because the tempting reading is the wrong one. Both layers separate the four groups strongly, with group-level R^2 values of 0.562 and 0.635, and both do so on the same structure.[32,33] They do not, however, couple at the level of the individual animal, and no Mantel or Procrustes variant tested here reaches significance.[34] Exhaustive within-group reassignment settles the most obvious objection: across all 1,296 possible re-pairings the Procrustes statistic never exceeded 0.351, so no assignment of the available animals — including the correct one — would have produced sample-level coupling. With three animals per arm and between-group effects this strong, the two layers carry a shared treatment structure rather than a shared individual axis. This is a finding about the level at which multi-omics agreement operates in a design of this size, and it is not a statement that the two datasets are inconsistent.

The cytokine readout shows that the shift accompanying ablation is registered in the compartment where the infection resides. Ablation was accompanied by the lowest IFN-γ and IL-10 levels and the highest TNF-α and IL-6 levels among the four arms, and the same pattern held in bronchoalveolar lavage fluid and in serum. The concordance across compartments is the observation that matters for the framing of this study: whatever the ablated gut community is doing to the host, it is legible at the mucosal surface of the lung and in the circulation at the same time, which is the pattern a gut–lung axis would generate and not the pattern a purely local pulmonary effect would.[1,2,35] The four analytes did not all move in the same direction within the pro-inflammatory set, so the panel is best read analyte by analyte rather than as a single index.

The boundaries of the study follow from its construction. Three animals per arm set the resolution of every group-level comparison, and the arm-level contrasts are reported at that resolution. The analytical window excludes short-chain fatty acids and polyamines, in negative mode on mass grounds and in positive mode on retention-time grounds, so no claim is made about either class; lactate is reported on accurate mass and retention time.[36] The metabolome that is degenerate in the ablated arm cannot be used to test whether the two layers couple under ablation, because the features in question are zero by definition rather than by measurement.

What would move this work forward is a design that keeps the specificity gain while raising resolution. A gnotobiotic arm colonised with a defined consortium would separate the loss of a community from the direct effects of the antibiotic,[15,27] and a targeted assay panel aimed at secondary bile acids, lignans and dicarboxylic acids would give the block a quantification the untargeted layer cannot. The natural next question is whether the metabolites that vanish under ablation are the ones that carry the cytokine shift, and that question is testable with the same four-arm frame.

Materials and Methods

Animals, infection and the four-arm design

Twelve mice were assigned to four arms of three animals each. All four arms shared a single BCG infection background. The arms were: untreated control (NC); BCG infection alone (BCG), which served as the comparator baseline for every other arm; BCG infection after mixed-antibiotic ablation of the gut community (ABX_BCG); and BCG infection followed by faecal microbiota transplantation (BCG_FMT). The ablated arm received antibiotics and the transplanted arm did not; the two were run as independent branches off the infected baseline, not as successive stages of one depletion-then-restoration procedure. Mice were C57BL/6, SPF grade, male, 6–8 weeks old and 18–22 g. On arrival they were housed in separate cages in a temperature-controlled animal room under a 12 h light/12 h dark cycle with free access to standard clean-grade chow and purified water, and were allowed 3 days to acclimatise before the experiment began. All animals were obtained from the Laboratory Animal Centre of Xinjiang Hospital of Beijing Children's Hospital; none of the animals used here was privately owned by an individual, another institution or a farm. BCG was the Danish 1331 strain, resuspended in sterile saline

and administered by intraperitoneal injection at 100 uL per mouse once weekly for two consecutive weeks, with the untreated control arm receiving the same volume of sterile saline by the same route; the mixed-antibiotic regimen was vancomycin 0.5 g/L, ampicillin 1 g/L, neomycin 1 g/L and metronidazole 1 g/L in drinking water, which the ablated arm received ad libitum for two weeks before BCG inoculation; faecal microbiota transplantation used fresh faeces from healthy donors of the same strain, homogenised in sterile PBS at 100 mg/mL, filtered through a 70 um mesh and given to each recipient as 200 uL by oral gavage after BCG infection.

Anaesthesia and euthanasia. Where anaesthesia was required, mice were anaesthetised with isoflurane carried in oxygen: induction at 3% (v/v) for approximately 3 min in an induction chamber, followed by maintenance at 1.5–2% (v/v) through a nose cone. Depth of anaesthesia was confirmed by loss of the pedal withdrawal reflex before any procedure was begun, and each animal was returned to a warmed cage and observed until it had regained sternal recumbency. At the end of the experiment, animals were anaesthetised to surgical depth with isoflurane as described above and then euthanised by cervical dislocation; death was confirmed by absence of a heartbeat and of spontaneous respiration before any tissue or fluid was collected. Anaesthesia was induced ahead of cervical dislocation so that the animals were unconscious at the point of death. Ethical approval was granted by the Institutional Animal Care and Use Committee of Xinjiang Hospital of Beijing Children's Hospital under approval number KY2025022719, and all procedures followed the applicable institutional guidelines for the care and use of laboratory animals. No injectable anaesthetic was used in this study; anaesthesia was maintained by the inhalation route only.

□醉与安乐死。 □要麻醉的操作中，小鼠以氧气携带的异氟烷吸入麻醉：诱导浓度 3%(v/v)、于诱导箱中约 3 min，随后经面罩维持 1.5–2%‰v/v₹◦开始任何操作之前，均以趾间反射消失确认麻醉深度；操作结束后将动物移回加温笼具，观察至其恢复胸骨着地姿势。实验结束时，先以上述方式用异氟烷麻醉至外科深度，再以颈椎脱臼处死∞在采集任何组织或体液之前，均以心跳与自主呼吸停止确认死亡。先麻醉后脱臼的顺序保证动物在死亡时处于无意识状态。动物伦理批号为北京儿童医院新疆医院实验动物伦理委员会 KY2025022719，全部操作遵循适用的实验动物护理与使用机构准则。

Metagenomic sequencing and community profiling

Twelve samples were subjected to shotgun metagenomic sequencing: NC_1/2/3, BCG_1/2/3, ABX_BCG_1/2/3 and BCG_FMT_1/2/3. In the delivered sequencing output the infected baseline samples are named BGC; throughout this manuscript that arm is written **BCG**, and it is the same group of animals as the metabolomic arm labelled BCG. Libraries were prepared and sequenced by Majorbio Biotech (Shanghai, China; contract MJ20260301026) on the Illumina platform in 2 × 150 bp paired-end mode, giving 40–46 million raw reads (6.1–7.0 Gb) per sample, with Q30 ≥ 96% after filtering. Raw reads were quality-controlled with fastp v0.20.1[37] (3' and 5' adapters trimmed; reads with mean quality < 20 or shorter than 50 bp after trimming discarded), after which host sequences were removed by mapping to the mouse genome with BWA v0.7.9a at default settings.[38] Clean reads were assembled individually per sample, discarding contigs shorter than 500 bp, which yielded N50 values of 3.2–6.8 kb. Open reading frames ≥ 100 bp were predicted with MetaGene/Prodigal v2.6.3,[39,40] and the predicted genes were clustered with CD-HIT at 90% identity and 90% coverage,[41] keeping the longest sequence of each cluster, to build a non-redundant gene catalogue of 970,271 genes (total length 744,429,090 bp; mean 767.24

bp). Gene abundances were obtained by aligning each sample's clean reads to the catalogue with SOAPaligner.[42] Taxonomic assignment used DIAMOND blastp ($E \leq 1 \times 10^{-5}$)[43] against the NCBI NR protein database, with gene abundances summed to the Domain, Kingdom, Phylum, Class, Order, Family, Genus and Species levels; the same DIAMOND search was run against eggNOG (COG), KEGG GENES, CAZy, ARDB, CARD and VFDB for functional annotation.[44–49] Relative abundances were computed at phylum, class, order, family, genus and species level from the taxonomic profile table delivered by the sequencing provider, the three ABX_BCG columns of which are mutually distinct (element-wise identity 29%, maximal difference $1.6–3.9 \times 10^5$; the three NC columns behave comparably at 19–22%), which is why n = 3 is used for this arm throughout the statistics.

Alpha diversity was computed as Shannon index and observed species count, and is reported for the three arms that retained a detectable community; the ablated arm has no community to profile. Beta diversity used genus-level Bray–Curtis dissimilarities[50] and principal coordinates analysis, with permutational multivariate analysis of variance (PERMANOVA)[51] over the same three arms at n = 3 each. Functional potential was summarised as KEGG level-3 pathway abundances, row-scaled to z-scores for display, with the ablated arm represented by a mean column. Differential taxa were identified with a rank-wise scoring procedure across the six taxonomic ranks, and genus-level effect sizes were expressed as log2 fold changes against the untreated control.

Metabolite extraction and LC-MS acquisition

Twelve biological samples plus three quality-control injections (QC01/02/03) were analysed on a SCIEX instrument in both positive and negative electrospray polarity, giving fifteen injections per mode. Separation used a Waters ACQUITY UPLC system with water (A) and acetonitrile (B) at a flow rate of 0.400 mL/min, a column temperature of 45°C and a sample temperature of 10°C, over a 12.00 min run: 0–0.20 min 100% A; 0.20–3.00 min to 75% A; 3.00–9.00 min to 0% A (100% B); 9.00–10.00 min held at 100% B; 10.10 min back to 100% A; 12.00 min end of run. Mass spectrometry used a SCIEX TripleTOF 6600 quadrupole time-of-flight instrument (serial number DW20161801) with an electrospray ionisation source under Analyst control. Samples were extracted with pre-chilled methanol/acetonitrile (1:1, v/v) containing internal standards. The analytical column was a Waters ACQUITY UPLC HSS T3 column (1.8 um, 2.1 x 100 mm) and the injection volume was 2 uL. Acquisition was data-dependent, collecting MS1 and MS2 spectra (approximately 1,677 MS1 and 11,773 MS2 spectra), which is the condition under which spectral-library annotation becomes possible.

Peak extraction

Raw .wiff files were converted to mzML with ProteoWizard msconvert in profile mode[52] and then centroid-detected with the peakPicking cwt algorithm. Features were extracted with asari.[53] The parameters that determine the result are worth stating explicitly, because the defaults are not what was used. Negative mode used the v8c parameter set with mz_tolerance_ppm = 10, returning 9,706 features and capturing 90.8% of quality-control signal. Positive mode used the v8d parameter set with

mz_tolerance_ppm = 20, returning 11,589 features and capturing 96.6% of quality-control signal. Both modes used rt_align_on = true and peak_number_rt_calibration = 1.

The tolerance in each mode was set to cover the measured m/z drift span across injections rather than chosen by convention: 6.87 ppm measured in negative mode and 17.43 ppm in positive mode, against which the applied windows of 10 ppm and 20 ppm were set. The reason positive mode needed the wider window is a matter of mass calibration, not of chromatography. Across injections the m/z axis drifted by as much as 17.43 ppm, and the three quality-control injections alone spanned 6.6 ppm of that drift; in contrast, the apex retention time of a given feature moved by only 2.33 s, or 0.32%, across injections. The fragmentation of positive-mode features was therefore driven by m/z calibration drift. Widening the window accordingly raised captured signal from 57.3% to 96.6%, lowered the share of signal sitting in fragmented features from 53.8% to 0.1%, and improved quality-control log-scale correlation from r = 0.74–0.80 to r = 0.90–0.91 (Spearman 0.49–0.55 to 0.90).

Quality control and normalisation

Samples were ordered using complete-case features only, that is, features detected across all fifteen injections: 431 features in negative mode and 783 in positive mode. Ordering on a matrix in which missing values had been replaced by a detection-limit surrogate was rejected as a basis for quality assessment, because it pushes the quality-control injections — the only samples that detect every feature — to the extreme of each missingness axis and makes a stable instrument look as if it had failed. Their apparent distance from the nearest group centroid under that treatment was 64.2 units in negative mode and 70.3 units in positive mode; on complete-case features, within-quality-control dispersion was 0.13 against within-group dispersions of 1.15–4.36 in negative mode, and 0.31 against 3.17–6.46 in positive mode.

Normalisation used probabilistic quotient normalisation (PQN).[54] The normalisation factors were measured rather than assumed to be neutral across groups, and they were not: in negative mode they ranged over 0.800–1.009 (NC), 0.906–1.182 (BCG), 1.000–1.032 (ABX_BCG), 1.051–1.190 (BCG_FMT) and 0.985–1.000 (QC); in positive mode over 0.867–1.001 (NC), 0.895–1.080 (BCG), 0.954–1.000 (ABX_BCG), 1.018–1.115 (BCG_FMT) and 1.000–1.032 (QC). No group was designated as a normalisation reference, and the measured ranges are reported in the display rather than replaced by an assumption of between-group neutrality.

Annotation and confidence tiers

Annotation used MS2 spectral libraries MASSBANK, BILELIB19 and GNPS-LIBRARY,[55,56] each trimmed to a precursor m/z window of ± 0.03 Da before matching. Scoring used a modified cosine metric that includes neutral-loss pairing, with TOL 0.02 and MIN_PEAKS 3. Of the features carrying MS2 spectra, 2,498 in negative mode and 3,063 in positive mode, 369 and 1,555 respectively returned a library hit. Identification confidence is reported as a tier rather than as a binary. Library-matched features carry the highest support; lactate in negative mode is reported on accurate mass (m/z 89.0251, + 7.9 ppm) and

retention time (67.0 s) without a library match in either polarity, and is treated as a lower confidence tier accordingly. Deoxycholic acid and chenodeoxycholic acid are isobaric at m/z 391.2828 with a common retention time of 437.9 s; the two cannot be separated by the acquisition used here and are reported as a pair.

Targeted analysis and coverage of the analytical window

Targeted screening was scored against a curated set of compounds and reported on a 0–1 scale. In negative mode five targets exceeded 0.70: tryptophan 0.974, taurocholate 0.972, cholate 0.953, the deoxycholate/chenodeoxycholate pair 0.945 and malate 0.747. In positive mode no target reached 0.70; indole-3-aldehyde scored 0.675, cholate 0.539 and indole 0.369. Secondary bile acids were called by detection rather than by score, since they were absent from one arm entirely. The coverage of the analytical window was characterised explicitly so that the absence of short-chain fatty acids and polyamines could be attributed to the method rather than read as biology. In negative mode the lowest recorded m/z was 71.0, which is 22,700 ppm from the nearest short-chain fatty acid ion, far outside the 10 ppm window. In positive mode the lowest recorded m/z was 57.0, within 24.7 ppm of the nearest candidate and therefore admissible on mass inside the 20 ppm window; that candidate elutes at 6.5 min, whereas the measured small polar acids elute before 1.1 min (lactate at 0.6, 0.9 and 1.1 min; malate at 0.65 min; 2-oxoglutarate at 1.05 min), so the exclusion in that mode is made on retention time.

Differential analysis and statistics

Differential analysis used limma[57] on features detected in every group, with Benjamini–Hochberg control of the false discovery rate. Features were called differentially abundant at FDR < 0.05 and |log2FC| ≥ 1. Block features — those recorded at 0.0% in all three ablated samples — are by construction excluded from limma, because the procedure requires detection in every group, and they therefore carry no log2 fold change. The per-comparison tables retain a detection-limit surrogate column in which an undetected feature is assigned 0.5 times its minimum observed value; that column must be read together with the accompanying detection column and was not used on its own for any claim in this manuscript. The denominator shown on the volcano displays is the number of tested features, which is smaller than the total row count because rows without a finite test statistic were removed; every such row belongs to the block bucket, which is a consequence of the detection requirement and is unrelated to the three contrasts.

Group-level separation of the metabolome was assessed by PERMANOVA on the all-feature matrix under total-sum scaling with Bray–Curtis distances; the flora-dependent subset was not used for ordination, because those features are zero across the ablated arm and their Bray–Curtis sample rows are degenerate by definition. Mantel and Procrustes statistics were computed between genus-level community distances and metabolome distances in several variants: all features with total-sum scaling and Bray–Curtis; features detected in at least six of twelve samples; flora-dependent features on a Euclidean log10 scale; the nine non-ablated samples only; and the last two restrictions combined. Pairwise associations between genus abundances and metabolite intensities used Spearman

correlation, with significance thresholds of $|\rho| \geq 0.577$ at $n = 12$ and $|\rho| \geq 0.667$ at $n = 9$ ($P < 0.05$). To test whether the low sample-level agreement could be attributed to mispaired samples, all $6^4 = 1{,}296$ within-group reassignments of the twelve animals were enumerated and the Procrustes statistic recomputed for each. Lactate intensity was compared across the four arms by Kruskal–Wallis test.

Cytokine quantification

Cytokines were quantified in bronchoalveolar lavage fluid and in serum by enzyme-linked immunosorbent assay, four analytes per compartment: IFN-γ, IL-10, TNF-α and IL-6, with three animals per arm. Commercial mouse ELISA kits for IFN-γ, IL-10, TNF-α and IL-6 were used, all according to the manufacturers' instructions, with samples diluted as recommended and standard curves fitted over the recommended range. Significance brackets were drawn for the three planned pairwise comparisons within each panel; absolute concentrations for every animal and analyte are provided in the source data file submitted with the manuscript.

Conclusion

In a four-arm mouse model sharing a single BCG infection background, mixed-antibiotic ablation of the gut community defined a block of 726 negative-mode and 313 positive-mode metabolite features that no ablated sample contained and that were detected in 88–94% of the remaining samples, with total ion signal in the ablated arm above that of the quality-control injections. Twenty-seven features of the block were annotated to 17 unique InChIKeys, 21 of them in compound classes of microbial origin, and the block was confirmed in a targeted layer by the complete absence of secondary bile acids from the ablated arm and by cross-channel agreement on deoxycholic acid. Running the ablated and transplanted arms as independent branches off the infected baseline is what makes this an antibiotic-specific control rather than a correlate of infection, and the two omics layers were found to carry a shared treatment structure rather than a shared individual axis. The cytokine readout places the same arm at the extreme of four analytes in both lung and blood. The block is defined by detection rather than by effect size, which ties it to the ablated state specifically rather than to infection or to transplantation, and the four-arm frame is now positioned to ask which of those metabolites, if any, carry the accompanying immune shift.

Declarations

Ethics approval and consent to participate. This study used animals and did not involve human participants: no human subjects, human tissue or human-derived material were used, so informed consent to participate was not applicable, and none was required or obtained. The animals used were obtained from the Laboratory Animal Centre of Xinjiang Hospital of Beijing Children's Hospital and were not privately owned by any individual, institution or farm, so consent from owners was not applicable. All animal procedures — infection, mixed-antibiotic treatment, faecal microbiota transplantation, anaesthesia and euthanasia — were approved in advance by the Institutional Animal Care and Use Committee of Xinjiang Hospital of Beijing Children's Hospital (approval number KY2025022719), and

were carried out in accordance with the guidelines of that committee and with the national regulations of the People's Republic of China governing the care and use of laboratory animals (GB/T 35892-2018). No additional permits or licences were required for the specimens reported here: faeces, serum, bronchoalveolar lavage fluid and lung tissue were all collected from the animals held under the approval named above, and no specimen was collected from the field or from any other source. The anaesthesia and euthanasia procedures are described under Animals, infection and the four-arm design in the Materials and Methods.

Consent for publication. Not applicable.

Availability of data and materials. The raw metagenomic and metabolomic data generated in this study, together with the processed feature tables, the differential-analysis result tables and the analysis scripts, are available from the corresponding authors upon reasonable request.

Competing interests. The authors declare that they have no competing interests.

Funding. This work was supported by the Key Research and Development Programme of Xinjiang Uygur Autonomous Region (2025B03020-2 and 2024B03021-2), the National Natural Science Foundation of China (82460003), and the following Xinjiang Second Medical College grants: XGGK2025-01, ZR202505, KT202507, XKZ202502 and ZR202529.

Authors' contributions. Yujie Ma, Lili Zhu and Yu Xie contributed equally to this work and share first authorship. Jiangdong Wu, Le Zhang and Qifeng Li conceived and designed the study, supervised the work and secured funding. Yujie Ma performed the animal experiments, processed the metabolomics samples and analysed the metabolomics data. Lili Zhu analysed and visualised the metagenomic data. Yu Xie performed the cytokine assays and compiled the results. Yuxuan Gou, Beiming Zhang, Rong Zhang, Chunhong Xiao and Jing Chen contributed to sample collection, laboratory assays and data verification. All authors drafted or critically revised the manuscript and approved the final version.

Acknowledgements. The authors thank the Laboratory Animal Centre of Xinjiang Hospital of Beijing Children's Hospital for animal husbandry and ethics review, the sequencing service provider for metagenomic sequencing and bioinformatic analysis, and Xinjiang Second Medical College and Shihezi University School of Medicine for experimental platform and funding support.

Declaration of generative AI use

During the preparation of this work the authors used a large language model to assist with language editing and translation. After using this tool, the authors reviewed and edited the content as needed and take full responsibility for the content of the publication.

References

1. Enaud R, Prevel R, Ciarlo E, Beaufils F, Wieërs G, Guery B, et al. The gut-lung axis in health and respiratory diseases: a place for inter-organ and inter-kingdom crosstalks. Front Cell Infect Microbiol. 2020;10:9. 10.3389/fcimb.2020.00009.
2. Wang L, Cai Y, Garssen J, Henricks PAJ, Folkerts G, Braber S. The bidirectional gut-lung axis in chronic obstructive pulmonary disease. Am J Respir Crit Care Med. 2023;207(9):1145–60. 10.1164/rccm.202206-1066TR.
3. Jin C, Lagoudas GK, Zhao C, Bullman S, Bhutkar A, Hu B, et al. Commensal microbiota promote lung cancer development via γδ T cells. Cell. 2019;176(5):998–e101316. 10.1016/j.cell.2018.12.040.
4. Kim SH, White Z, Gainullina A, Kang S, Kim J, Dominguez JR, et al. IL-10 sensing by lung interstitial macrophages prevents bacterial dysbiosis-driven pulmonary inflammation. Immunity. 2025;58(5):1306–e267. 10.1016/j.immuni.2025.04.004.
5. Lynn DJ, Benson SC, Lynn MA, Pulendran B. Modulation of immune responses to vaccination by the microbiota: implications and potential mechanisms. Nat Rev Immunol. 2022;22(1):33–46. 10.1038/s41577-021-00554-7.
6. Hagan T, Cortese M, Rouphael N, Boudreau C, Linde C, Maddur MS, et al. Antibiotics-driven gut microbiome perturbation alters immunity to vaccines in humans. Cell. 2019;178(6):1313–e2813. 10.1016/j.cell.2019.08.010.
7. Chen J, Gao L, Wu X, Fan Y, Liu M, Peng L, et al. BCG-induced trained immunity: history, mechanisms and potential applications. J Transl Med. 2023;21(1):106. 10.1186/s12967-023-03944-8.
8. Kaufmann E, Sanz J, Dunn JL, Khan N, Mendonça LE, Pacis A, et al. BCG educates hematopoietic stem cells to generate protective innate immunity against tuberculosis. Cell. 2018;172(1–2):176–e9019. 10.1016/j.cell.2017.12.031.
9. Chai Y, Li M, Deng X, Ma C, Zhou N, Chen Y, et al. Gut microbiota and tuberculosis infection: interaction and therapeutic potential. Gut Microbes. 2025;17(1):2531201. 10.1080/19490976.2025.2531201.
10. Maier L, Goemans CV, Wirbel J, Kuhn M, Eberl C, Pruteanu M, et al. Unravelling the collateral damage of antibiotics on gut bacteria. Nature. 2021;599(7883):120–4. 10.1038/s41586-021-03986-2.
11. Perdijk O, Butler A, Macowan M, Chatzis R, Bulanda E, Grant RD, et al. Antibiotic-driven dysbiosis in early life disrupts indole-3-propionic acid production and exacerbates allergic airway inflammation. Immunity. 2024;57(8):1939–e547. 10.1016/j.immuni.2024.06.010.
12. Yang M, Zheng X, Fan J, Cheng W, Yan TM, Lai Y, et al. Antibiotic-induced gut microbiota dysbiosis modulates host transcriptome and m6A epitranscriptome via bile acid metabolism. Adv Sci (Weinh). 2024;11(28):e2307981. 10.1002/advs.202307981.
13. Kappel BA, De Angelis L, Puetz A, Ballanti M, Menghini R, Marx N, et al. Antibiotic-induced gut microbiota depletion exacerbates host hypercholesterolemia. Pharmacol Res. 2023;187:106570. 10.1016/j.phrs.2022.106570.
14. Bokoliya SC, Dorsett Y, Panier H, Zhou Y. Procedures for fecal microbiota transplantation in murine microbiome studies. Front Cell Infect Microbiol. 2021;11:711055. 10.3389/fcimb.2021.711055.

15. Cheng AG, Ho PY, Aranda-Díaz A, Jain S, Yu FB, Meng X, et al. Design, construction, and in vivo augmentation of a complex gut microbiome. Cell. 2022;185(19):3617–e3619. 10.1016/j.cell.2022.08.003.
16. Porcari S, Benech N, Valles-Colomer M, Segata N, Gasbarrini A, Cammarota G, et al. Key determinants of success in fecal microbiota transplantation: from microbiome to clinic. Cell Host Microbe. 2023;31(5):712–33. 10.1016/j.chom.2023.03.020.
17. Tan J, Gong J, Liu F, Li B, Li Z, You J, et al. Evaluation of an antibiotic cocktail for fecal microbiota transplantation in mouse. Front Nutr. 2022;9:918098. 10.3389/fnut.2022.918098.
18. Yadegar A, Bar-Yoseph H, Monaghan TM, Pakpour S, Severino A, Kuijper EJ, et al. Fecal microbiota transplantation: current challenges and future landscapes. Clin Microbiol Rev. 2024;37(2):e0006022. 10.1128/cmr.00060-22.
19. DeLeon O, Mocanu M, Tan A, Sidebottom AM, Koval J, Ceccato HD, et al. Microbiome mismatches from microbiota transplants lead to persistent off-target metabolic and immunomodulatory effects. Cell. 2025;188(15):3927–e4113. 10.1016/j.cell.2025.05.014.
20. Ridlon JM, Kang DJ, Hylemon PB. Bile salt biotransformations by human intestinal bacteria. J Lipid Res. 2006;47(2):241–59. 10.1194/jlr.R500013-JLR200.
21. Funabashi M, Grove TL, Wang M, Varma Y, McFadden ME, Brown LC, et al. A metabolic pathway for bile acid dehydroxylation by the gut microbiome. Nature. 2020;582(7813):566–70. 10.1038/s41586-020-2396-4.
22. Kim KH, Park D, Jia B, Baek JH, Hahn Y, Jeon CO. Identification and characterization of major bile acid 7α-dehydroxylating bacteria in the human gut. mSystems. 2022;7(4):e0045522. 10.1128/msystems.00455-22.
23. Yang Y, Gao W, Zhu R, Tao L, Chen W, Zhu X, et al. Systematic identification of secondary bile acid production genes in global microbiome. mSystems. 2025;10(1):e0081724. 10.1128/msystems.00817-24.
24. Osswald A, Wortmann E, Wylensek D, Kuhls S, Coleman OI, Peuker K, et al. Secondary bile acid production by gut bacteria promotes Western diet-associated colorectal cancer. Gut. 2026;75(8):1505–19. 10.1136/gutjnl-2024-332243.
25. Wang LQ, Meselhy MR, Li Y, Qin GW, Hattori M. Human intestinal bacteria capable of transforming secoisolariciresinol diglucoside to mammalian lignans, enterodiol and enterolactone. Chem Pharm Bull (Tokyo). 2000;48(11):1606–10. 10.1248/cpb.48.1606.
26. Dong J, Huang L, Wang C, Luo X, Wei J, Abuduxukuer K, et al. Dietary probiotic ingestion is associated with elevated enterolignans concentration in the United States population. Front Nutr. 2025;12:1527029. 10.3389/fnut.2025.1527029.
27. Woting A, Clavel T, Loh G, Blaut M. Bacterial transformation of dietary lignans in gnotobiotic rats. FEMS Microbiol Ecol. 2010;72(3):507–14. 10.1111/j.1574-6941.2010.00863.x.
28. Sinha SR, Haileselassie Y, Nguyen LP, Tropini C, Wang M, Becker LS, et al. Dysbiosis-induced secondary bile acid deficiency promotes intestinal inflammation. Cell Host Microbe.

2020;27(4):659–e705. 10.1016/j.chom.2020.01.021.

29. Hang S, Paik D, Yao L, Kim E, Trinath J, Lu J, et al. Bile acid metabolites control TH17 and Treg cell differentiation. Nature. 2019;576(7785):143–8. 10.1038/s41586-019-1785-z.
30. Arifuzzaman M, Won TH, Li TT, Yano H, Digumarthi S, Heras AF, et al. Inulin fibre promotes microbiota-derived bile acids and type 2 inflammation. Nature. 2022;611(7936):578–84. 10.1038/s41586-022-05380-y.
31. Su X, Gao Y, Yang R. Gut microbiota derived bile acid metabolites maintain the homeostasis of gut and systemic immunity. Front Immunol. 2023;14:1127743. 10.3389/fimmu.2023.1127743.
32. Liang X, Fu Y, Cao WT, Wang Z, Zhang K, Jiang Z, et al. Gut microbiome, cognitive function and brain structure: a multi-omics integration analysis. Transl Neurodegener. 2022;11(1):49. 10.1186/s40035-022-00323-z.
33. Rozera T, Pasolli E, Segata N, Ianiro G. Machine learning and artificial intelligence in the multi-omics approach to gut microbiota. Gastroenterology. 2025;169(3):487–501. 10.1053/j.gastro.2025.02.035.
34. Liang L, Kong C, Li J, Liu G, Wei J, Wang G, et al. Distinct microbes, metabolites, and the host genome define the multi-omics profiles in right-sided and left-sided colon cancer. Microbiome. 2024;12(1):274. 10.1186/s40168-024-01987-7.
35. Ziaka M, Exadaktylos A. Gut-derived immune cells and the gut-lung axis in ARDS. Crit Care. 2024;28(1):220. 10.1186/s13054-024-05006-x.
36. Broeckling CD, Beger RD, Cheng LL, Cumeras R, Cuthbertson DJ, Dasari S, et al. Current practices in LC-MS untargeted metabolomics: a scoping review on the use of pooled quality control samples. Anal Chem. 2023;95(51):18645–54. 10.1021/acs.analchem.3c02924.
37. Chen S, Zhou Y, Chen Y, Gu J. fastp: an ultra-fast all-in-one FASTQ preprocessor. Bioinformatics. 2018;34(17):i884–90. 10.1093/bioinformatics/bty560.
38. Li H, Durbin R. Fast and accurate short read alignment with Burrows-Wheeler transform. Bioinformatics. 2009;25(14):1754–60. 10.1093/bioinformatics/btp324.
39. Noguchi H, Park J, Takagi T. MetaGene: prokaryotic gene finding from environmental genome shotgun sequences. Nucleic Acids Res. 2006;34(19):5623–30. 10.1093/nar/gkl723.
40. Hyatt D, Chen GL, Locascio PF, Land ML, Larimer FW, Hauser LJ. Prodigal: prokaryotic gene recognition and translation initiation site identification. BMC Bioinformatics. 2010;11:119. 10.1186/1471-2105-11-119.
41. Fu L, Niu B, Zhu Z, Wu S, Li W. CD-HIT: accelerated for clustering the next-generation sequencing data. Bioinformatics. 2012;28(23):3150–2. 10.1093/bioinformatics/bts565.
42. Li R, Yu C, Li Y, Lam TW, Yiu SM, Kristiansen K, et al. SOAP2: an improved ultrafast tool for short read alignment. Bioinformatics. 2009;25(15):1966–7. 10.1093/bioinformatics/btp336.
43. Buchfink B, Xie C, Huson DH. Fast and sensitive protein alignment using DIAMOND. Nat Methods. 2015;12(1):59–60. 10.1038/nmeth.3176.

44. Powell S, Forslund K, Szklarczyk D, Trachana K, Roth A, Huerta-Cepas J, et al. eggNOG v4.0: nested orthology inference across 3686 organisms. Nucleic Acids Res. 2014;42(Database issue):D231–9. 10.1093/nar/gkt1253.
45. Kanehisa M, Furumichi M, Sato Y, Kawashima M, Ishiguro-Watanabe M. KEGG for taxonomy-based analysis of pathways and genomes. Nucleic Acids Res. 2023;51(D1):D587–92. 10.1093/nar/gkac963.
46. Drula E, Garron ML, Dogan S, Lombard V, Henrissat B, Terrapon N. The carbohydrate-active enzyme database: functions and literature. Nucleic Acids Res. 2022;50(D1):D571–7. 10.1093/nar/gkab1045.
47. Liu B, Pop M. ARDB–Antibiotic Resistance Genes Database. Nucleic Acids Res. 2009;37(Database issue):D443–7. 10.1093/nar/gkn656.
48. Alcock BP, Huynh W, Chalil R, Smith KW, Raphenya AR, Wlodarski MA, et al. CARD 2023: expanded curation, support for machine learning, and resistome prediction at the Comprehensive Antibiotic Resistance Database. Nucleic Acids Res. 2023;51(D1):D690–9. 10.1093/nar/gkac920.
49. Liu B, Zheng D, Zhou S, Chen L, Yang J. VFDB 2022: a general classification scheme for bacterial virulence factors. Nucleic Acids Res. 2022;50(D1):D912–7. 10.1093/nar/gkab1107.
50. Bray JR, Curtis JT. An ordination of the upland forest communities of southern Wisconsin. Ecol Monogr. 1957;27(4):325–49. 10.2307/1942268.
51. Anderson MJ. A new method for non-parametric multivariate analysis of variance. Austral Ecol. 2001;26(1):32–46. 10.1046/j.1442-9993.2001.01070.x.
52. Chambers MC, Maclean B, Burke R, Amodei D, Ruderman DL, Neumann S, et al. A cross-platform toolkit for mass spectrometry and proteomics. Nat Biotechnol. 2012;30(10):918–20. 10.1038/nbt.2377.
53. Li S, Siddiqa A, Thapa M, Chi Y, Zheng S. Trackable and scalable LC-MS metabolomics data processing using asari. Nat Commun. 2023;14(1):4113. 10.1038/s41467-023-39889-1.
54. Dieterle F, Ross A, Schlotterbeck G, Senn H. Probabilistic quotient normalization as robust method to account for dilution of complex biological mixtures: application in 1H NMR metabonomics. Anal Chem. 2006;78(13):4281–90. 10.1021/ac051632c.
55. Horai H, Arita M, Kanaya S, Nihei Y, Ikeda T, Suwa K, et al. MassBank: a public repository for sharing mass spectral data for life sciences. J Mass Spectrom. 2010;45(7):703–14. 10.1002/jms.1777.
56. Wang M, Carver JJ, Phelan VV, Sanchez LM, Garg N, Peng Y, et al. Sharing and community curation of mass spectrometry data with Global Natural Products Social Molecular Networking. Nat Biotechnol. 2016;34(8):828–37. 10.1038/nbt.3597.
57. Ritchie ME, Phipson B, Wu D, Hu Y, Law CW, Shi W, et al. limma powers differential expression analyses for RNA-sequencing and microarray studies. Nucleic Acids Res. 2015;43(7):e47. 10.1093/nar/gkv007.

Figures

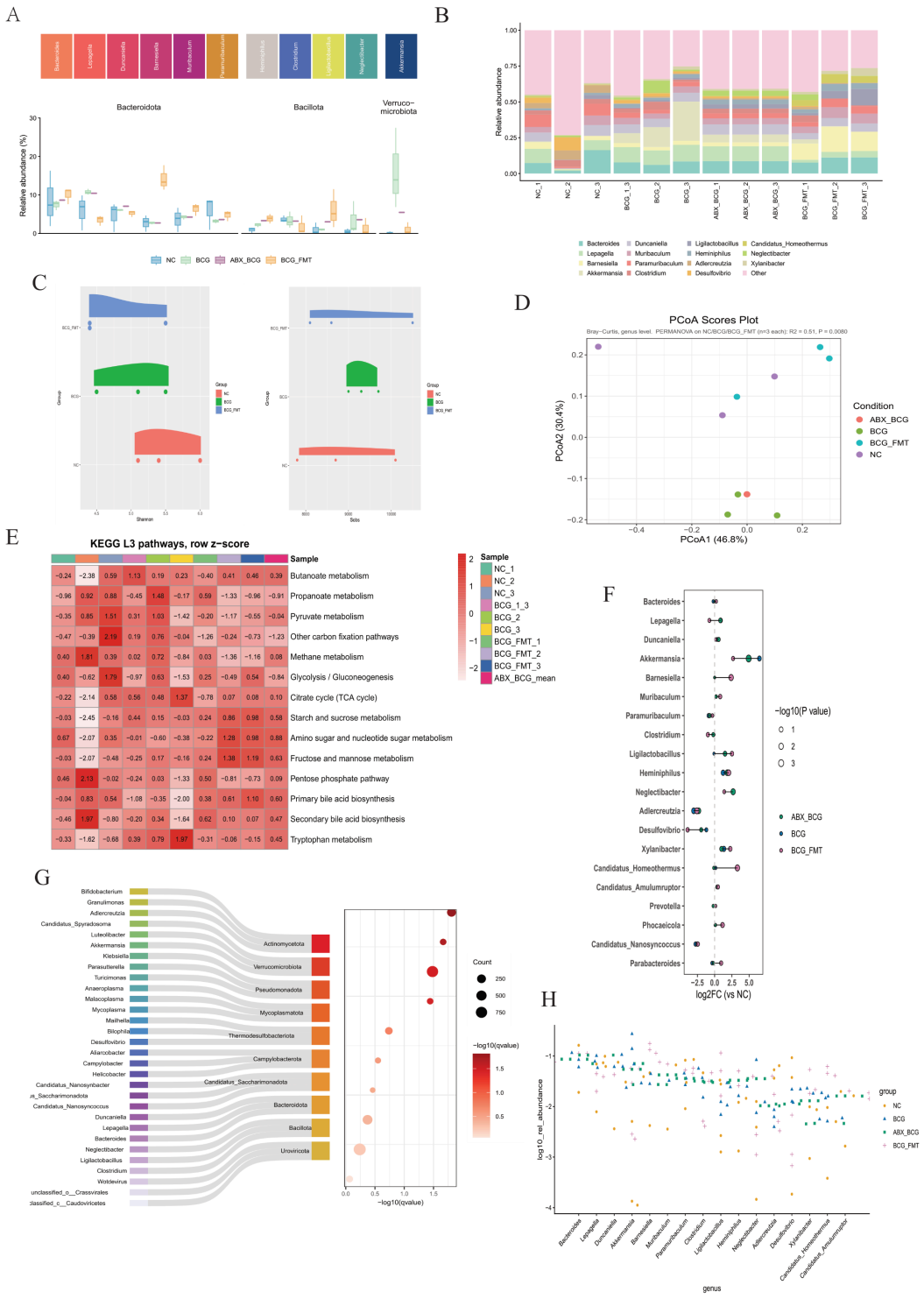

Figure 1

Community structure and functional potential across the four arms.

(A) Genus-level composition of each arm: relative abundance (%) of the eleven most abundant genera, grouped by phylum (Bacteroidota, Bacillota, Verrucomicrobiota), for NC, BCG, ABX_BCG and BCG_FMT (n = 3 per arm).

(B) Library-level composition: relative abundance of the fifteen most abundant taxa in each of the twelve individual libraries, with the remainder collapsed as "Other".

(C) Alpha diversity of the nine community-bearing libraries (NC, BCG and BCG_FMT; n = 3 each), shown as the Shannon index (axis 4.5–6.0) and observed richness (Sobs, axis 8000–10000).

(D) Genus-level Bray–Curtis ordination of the same nine libraries; PCoA 1 and PCoA 2 account for 46.8% and 30.4% of the variance, and PERMANOVA over the three community-bearing arms gives $R^2 = 0.51$ ($P = 0.0057$).

(E) Row z-scored relative abundance of fourteen KEGG level-3 metabolic pathways across the nine community-bearing libraries together with the ABX_BCG arm mean; the colour scale runs from −2 to 2.

(F) Genus-level effect sizes for the three contrasts against NC (ABX_BCG, BCG and BCG_FMT): the horizontal position gives the log2 fold change, the bubble size the −log10(P value) and the bubble colour the contrast.

(G) Two-level Sankey diagram resolving the ten phyla into their constituent genera; ribbon width scales with the associated count (250–750) and ribbon colour encodes −log10(q value) on a 0.0–1.5 scale.

(H) Genus-level relative abundance (log10) for the sixteen most abundant genera, one point per library, coloured by arm.

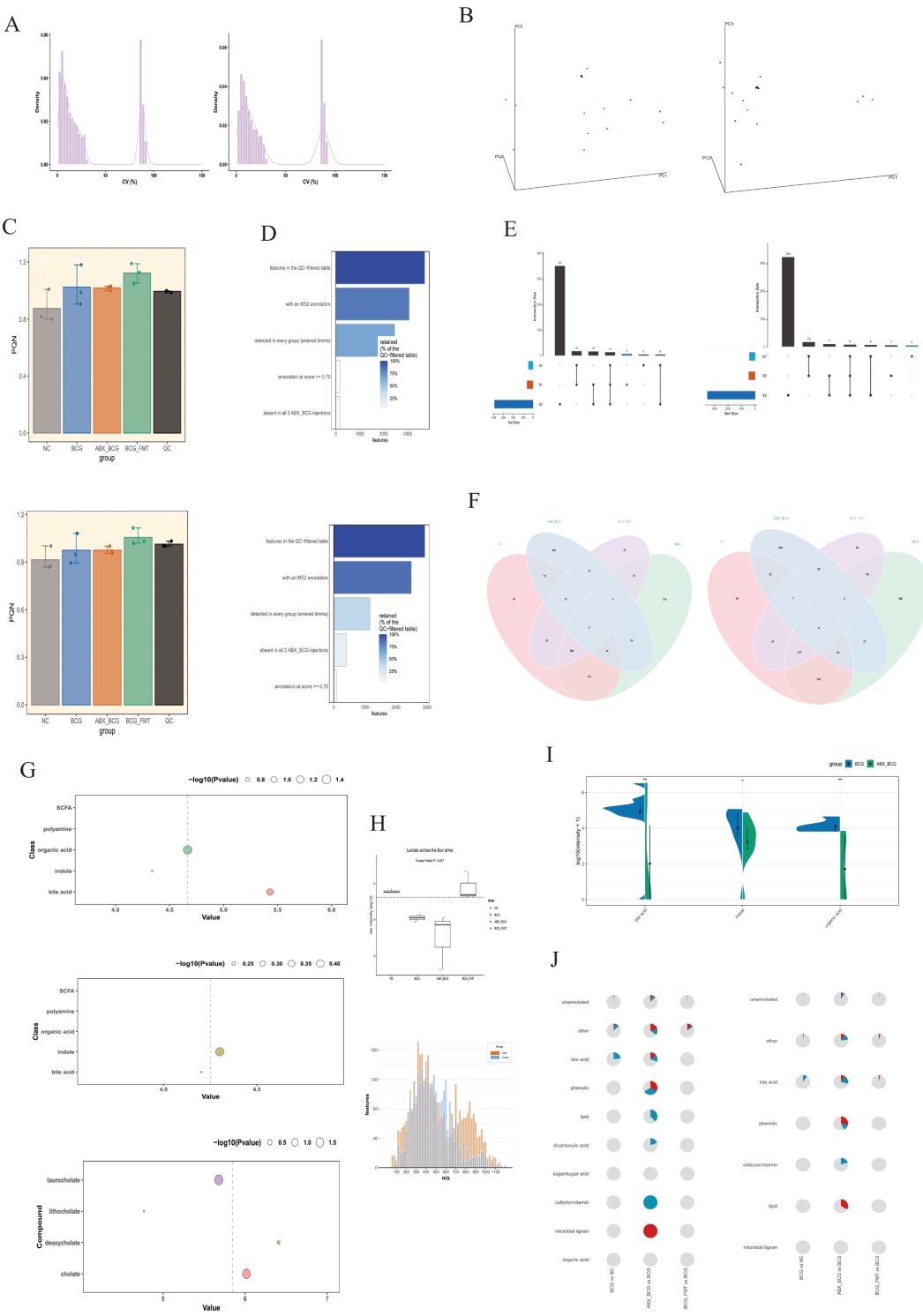

Figure 2

Metabolomic quality control and the differential feature set.

(A) Distribution of the coefficient of variation (%) across features, shown for both ionisation modes (NEG, POS); axis 0–150%.

(B) Three-dimensional PCA of the twelve samples in each ionisation mode (PC1, PC2 and PC3).

(C) PQN normalisation factors per sample in each ionisation mode (axis 0.0–1.2); NC, BCG, ABX_BCG, BCG_FMT and the pooled QC samples are distinguished.

(D) Feature-retention cascade for each ionisation mode: from the QC-filtered table, through features carrying an MS2 annotation, features detected in every group (entered limma) and annotations at score ≥ 0.70, down to features absent from all three ABX_BCG injections. The companion axis gives retention as a percentage of the QC-filtered table.

(E) UpSet plot of the differential feature sets for each ionisation mode (sets S1, S2 and S3); the largest intersection contains 352 features in NEG and 324 in POS.

(F) Detection of the differential features across the four arms in each ionisation mode, giving the number of features detected for each arm combination.

(G) Compound-class bubble plots: the five metabolite classes (SCFA, polyamine, organic acid, indole and bile acid) and the four bile acids (taurocholate, lithocholate, deoxycholate and cholate). Bubble position gives the value, bubble colour the −log10(P value), and both ionisation modes are shown.

(H) Left, lactate across the four arms (Kruskal–Wallis P = 0.047; y axis, raw intensity on a log10 scale). Right, the m/z coverage of the annotated features (x axis, m/z 100–1100; y axis, number of features), split into case and control.

(I) Bile acid, indole and organic acid intensities (log10(intensity + 1)) compared between the BCG and ABX_BCG arms.

(J) Annotation class × contrast cross-tabulation for both ionisation modes: the number of features in each annotated class (organic acid, microbial lignan, cofactor/vitamin, sugar/sugar acid, dicarboxylic acid, lipid, phenolic, bile acid, other and unannotated) is given for the BCG vs NC, ABX_BCG vs BCG and BCG_FMT vs BCG contrasts.

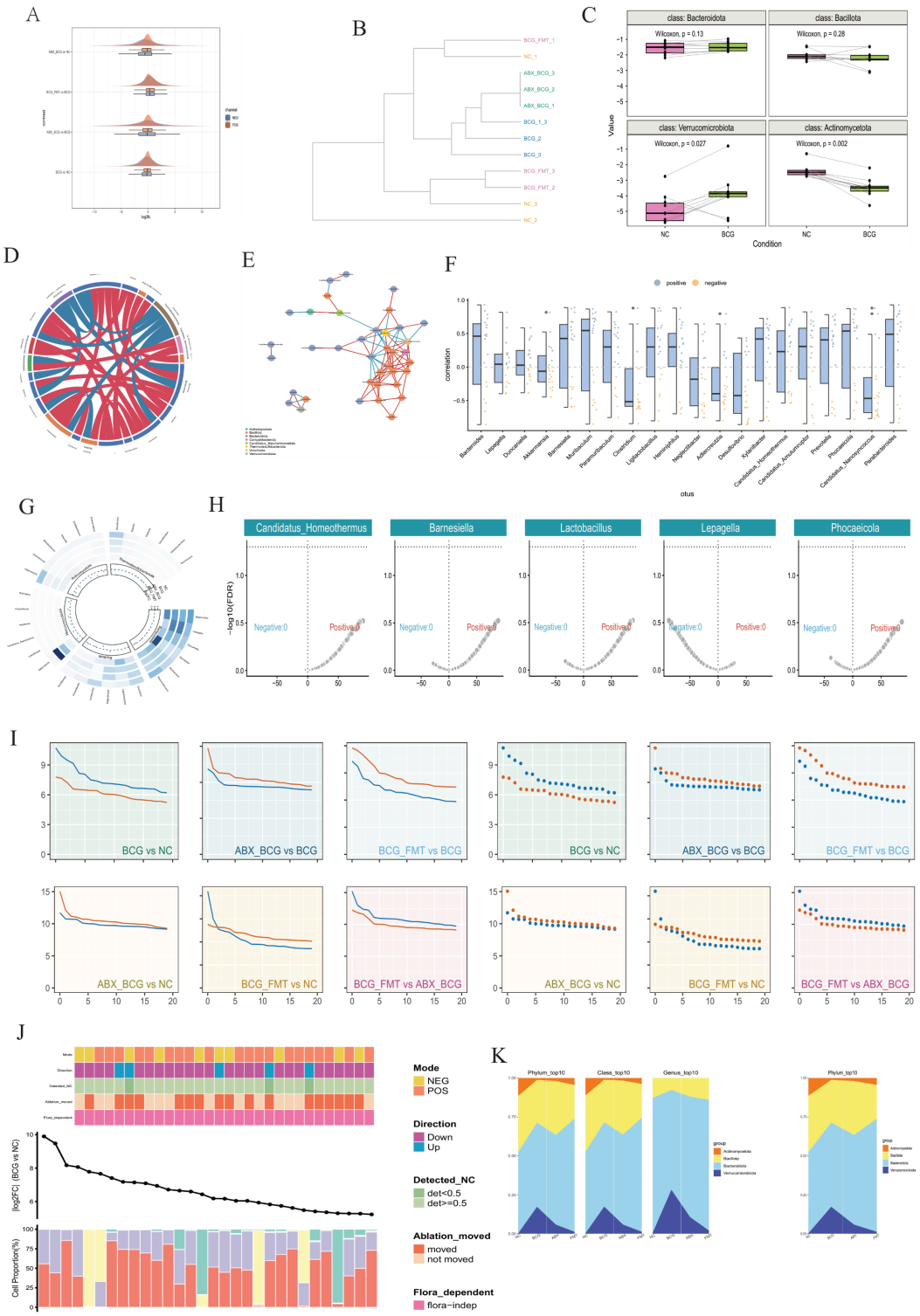

Figure 3

Contrast-specific effect sets differ in size and in composition.

(A) Distribution of per-feature log2 fold changes for each of the four contrasts (BCG vs NC, ABX_BCG vs BCG, BCG_FMT vs BCG and ABX_BCG vs NC), split by ionisation channel (NEG, POS); axis −10 to 10.

(B) Hierarchical clustering of the twelve libraries on their community profiles, with leaves labelled by library.

(C) Paired class-level abundances (NC versus BCG) for Bacteroidota, Bacillota, Verrucomicrobiota and Actinomycetota, with Wilcoxon signed-rank P values of 0.13, 0.28, 0.027 and 0.002 respectively.

(D) Chord diagram of the genus-level community structure across the twelve libraries; sectors are genera, labelled together with their phylum, and ribbon width reflects the weight of the corresponding association.

(E) Co-occurrence network of the most abundant genera, coloured by phylum; eight phyla are represented.

(F) Split-half reproducibility of the genus-level association estimates: for each of the twenty genera the correlation between the two halves is plotted, coloured by sign, on a −0.5 to 1.0 axis.

(G) Circular (circos) display of genus-level log2 fold changes for the four arms; ring segments are genera, ordered by phylum and coloured by arm.

(H) Facet volcano plots for the five genera with the largest genus-level effect sizes (Candidatus_Homeothermus, Barnesiella, Lactobacillus, Lepagella and Phocaeicola): the x axis is the log2 fold change (−50 to 50) and the y axis −log10(FDR) (0 to 1). No genus-level feature reached FDR significance in any facet, so each facet reads "Negative: 0 | Positive: 0".

(I) Feature counts for the six contrasts, shown for each ionisation channel; the y axes span 0–9 in the upper pairs and 0–20 in the lower pairs.

(J) Annotation summary of the differential features: for each feature class the panel reports the detection mode, the direction of change, whether it was detected in NC, whether antibiotic ablation moved it, and whether the response was flora-dependent. The left axis is |log2FC| (BCG versus NC) on a 6–10 scale and the right axis is cell proportion (%).

(K) Facet stacked area plots of community composition for the four arms at phylum, class and genus level (top ten taxa at each level).

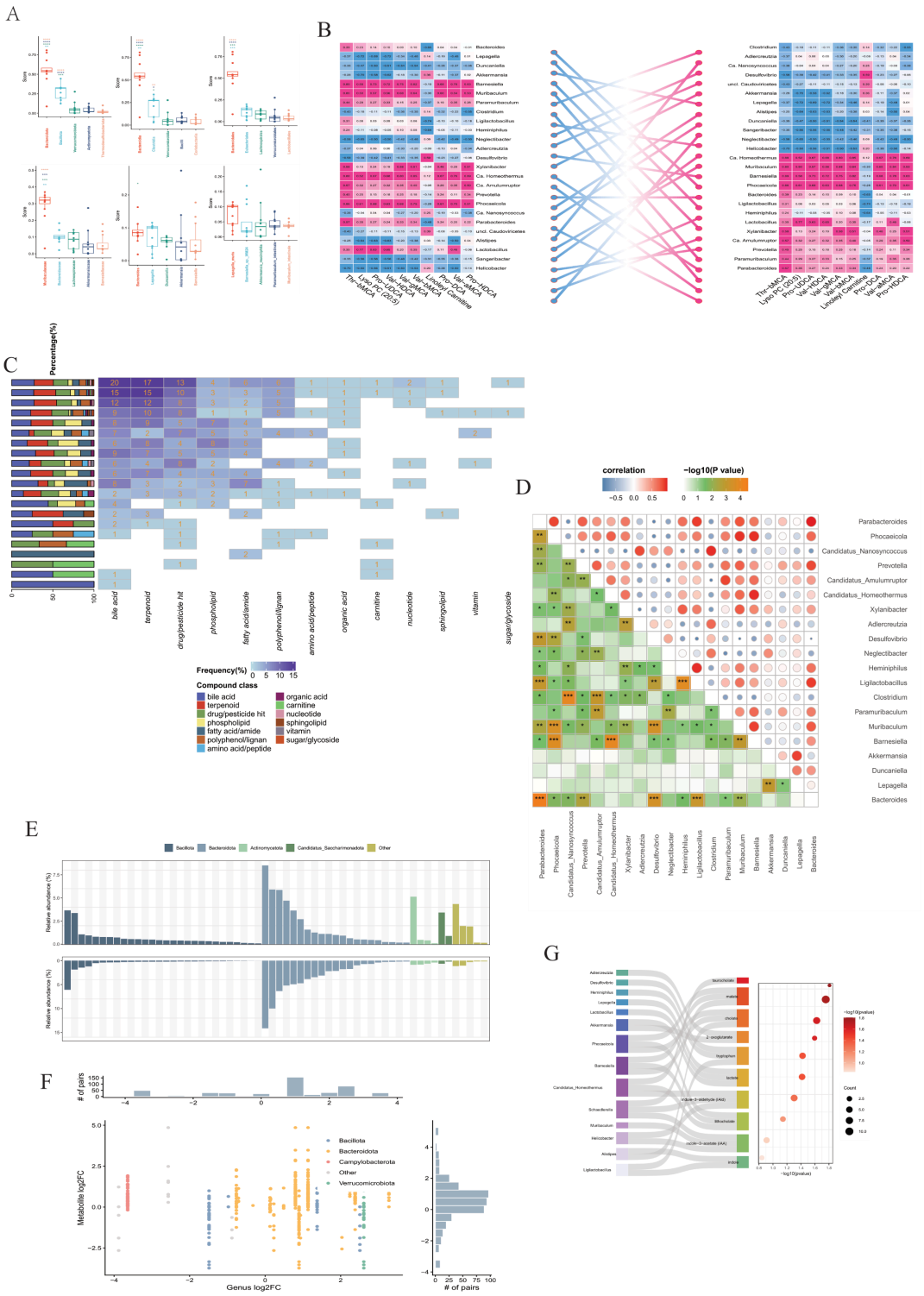

Figure 4

Differential scoring by taxonomic rank, genus–metabolite association, and the targeted layer.

(A) Differential Score at six taxonomic ranks — phylum, class, order, family, genus and species — for the five most abundant taxa at each rank; asterisks mark significance.

(B) Association between the 25 most abundant genera and the ten bile-acid and carnitine species retained from the targeted screen, displayed as a matrix of correlation values.

(C) Frequency of each compound class among the differential features: bile acid, terpenoid, drug/pesticide hit, phospholipid, fatty acid/amide, polyphenol/lignan, amino acid/peptide, organic acid, carnitine, nucleotide, sphingolipid, vitamin and sugar/glycoside. The left axis gives the percentage and the right axis the frequency.

(D) Genus × genus correlation matrix for twenty genera; colour encodes the correlation, bubble size the −log10(P value) and asterisks significance.

(E) Phylum- and genus-level community composition as stacked relative abundance; the phylum-level view is drawn on a 0–7.5% axis and the genus-level view on a 0–15% axis.

(F) Genus log2 fold change against metabolite log2 fold change for every retained genus–metabolite pair, coloured by phylum, with marginal distributions of the number of pairs.

(G) Association between the ten targeted compounds (taurocholate, malate, cholate, 2-oxoglutarate, tryptophan, lactate, indole-3-aldehyde, lithocholate, indole-3-acetate and indole) and their partner genera; bubble colour encodes −log10(P value) (0.8–1.8) and bubble size the count (2.5–10).

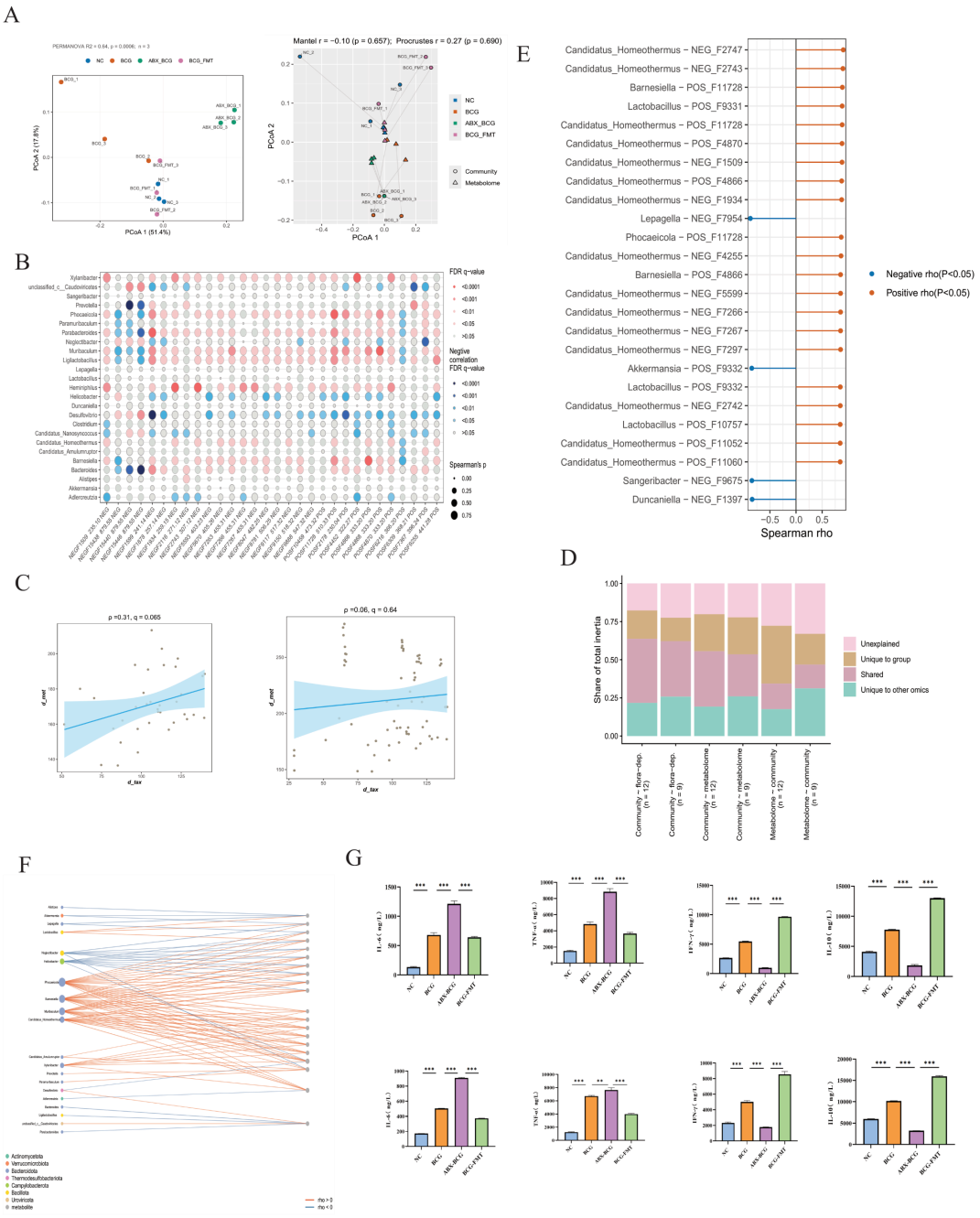

Figure 5

Agreement between the metagenomic and metabolomic layers, and the cytokine readout across two compartments.

(A) Ordination of the two layers on their own axes. Left, metabolome ordination of the twelve samples under total-sum scaling and Bray–Curtis; PCoA 1 and PCoA 2 account for 51.4% and 17.8% of the

variance, and PERMANOVA gives $R^2 = 0.64$ ($P = 0.0006$). Right, the community and metabolome point clouds superimposed in a common frame, with the layer-agreement statistics printed on the panel — Mantel $r = -0.10$ ($P = 0.657$) and Procrustes $r = 0.27$ ($P = 0.690$). Arms are coloured NC, BCG, ABX_BCG and BCG_FMT throughout; n = 3 per arm.

(B) Spearman correlation between the 25 most abundant genera and 30 metabolites, with FDR q-value stratification; rows and columns are ordered by the correlation structure.

(C) Distance–decay relation between community dissimilarity (d_tax, x axis) and metabolome dissimilarity (d_met, y axis), computed on the nine community-bearing samples (left; $\rho = 0.31$, $q = 0.065$) and on all twelve samples (right; $\rho = 0.06$, $q = 0.64$). Grey points are individual sample pairs; the line and band are the fitted trend and its uncertainty.

(D) Variance in the community and metabolome matrices attributable to flora-dependent features, shown for the n = 12 and n = 9 scans.

(E) The 25 strongest genus–metabolite pairs ranked by Spearman ρ; the dashed lines mark the significance threshold $|\rho| = 0.587$ at n = 12.

(F) Bipartite genus–metabolite network of the retained pairs; node colour encodes phylum and edge colour the sign of ρ.

(G) Cytokine readout: eight ELISAs covering four analytes in two compartments — top row, bronchoalveolar lavage fluid; bottom row, serum — with the columns ordered IL-6, TNF-α, IFN-γ and IL-10, and n = 3 animals per arm in every panel. ABX_BCG is the lowest arm for IFN-γ and IL-10 and the highest arm for TNF-α and IL-6. Brackets mark the three planned contrasts in each panel (NC versus BCG, BCG versus ABX_BCG, ABX_BCG versus BCG_FMT); all reached significance, with the serum TNF-α BCG-versus-ABX_BCG contrast at $P < 0.01$ and the remainder at $P < 0.001$. Absolute concentrations are given in the source data.